Investigation of divertor movement during disruptions in ASDEX Upgrade

M. Dibon[a], I. Zammuto[a], A. Herrmann[a], S. Vorbrugg[a], ASDEX Upgrade Team

[a]Max-Planck-Institute for Plasma Physics, Boltzmannstr. 2, 85748 Garching, Germany

The divertor serves as the main power exhaust of tokamaks. Hence the target tiles in the divertor must be carefully aligned to prevent leading edges which would result in higher power deposition and subsequent melting. The outer strike line in the lower divertor of ASDEX Upgrade is located on the assembly 1, which consists of the target tiles, the cooling plates and the support structure. Since the transition to the tungsten optimized divertor design of the divertor in 2014, it has been observed that the assembly 1 and the underlying frame are displaced over the course of an experimental campaign. The attachment of the assembly has been modified several times to prevent this displacement. However, a complete suppression of the movement was not achieved. The reason for the displacement is suspected to be due to induced currents and the resulting jxB forces during disruptions. This was investigated using a full 3D transient model of the ASDEX Upgrade coil system and a model of the assembly 1 with frame and vacuum vessel. The different assembly modifications and several current quench times were simulated, resulting in forces of up to 5.5 kN and torques up to 6.3 kNm. These forces were then used in a 3D transient structural model of the assembly to investigate the resulting displacements. It was found that displacements occur in all cases but they vary between 0.25 mm and 0.75 mm.

Keywords: divertor, disruption, electromagnetic force

I. INTRODUCTION

The divertor is an important component of most fusion devices, as it serves as power exhaust for the machine. This is achieved by diverting the plasma outside the last closed flux surface into an outer and inner leg which are then guided onto special target tiles. The strike lines, on which the plasma hits the tiles, are characterized by heat fluxes of up to 15 MW/m² in ASDEX Upgrade [1]. For this reason the tiles are either made of graphite [2] or tungsten [3] as these materials can withstand these heat fluxes. The alignment of the target tiles is also of great importance as leading edges are exposed to higher heat fluxes than the tile surface. This can lead to severe damage or destruction of entire tiles. For this reason, the tungsten divertor in ASDEX Upgrade (AUG) is carefully aligned after every maintenance break to prevent leading edges and to ensure proper shading across neighboring divertor assemblies. The divertor of AUG was originally equipped with graphite tiles. Since graphite is not suitable as target material for reactors, and thus for ITER, due to hydrogen co-deposition, AUG was stepwise transformed to a tungsten first wall [4]. The current design of the lower divertor (Div-III [5]), with solid tungsten tiles on the outer divertor, was introduced in 2014 to expand the experimental capabilities of AUG. Since this change it was observed that the divertor assembly 1, which holds the target tiles for the outer strike line, was displaced in radial direction during an experimental campaign. Fig. 1 shows the radial offsets of the assemblies with respect to their neighboring assemblies in each toroidal sector directly before and directly after the experimental campaign between February and July 2017, which stands exemplary for the behavior in the campaigns prior. The green line represents the status of the assemblies after maintenance and the red line indicates the positions directly after opening the machine. It can be seen that during the experiments displacements between 0 mm and 0.35 mm occurred. Depending on the direction of the displacement, this increased or decreased shading between the assemblies, resulting in leading edges, higher heat fluxes and partial melting of tiles.
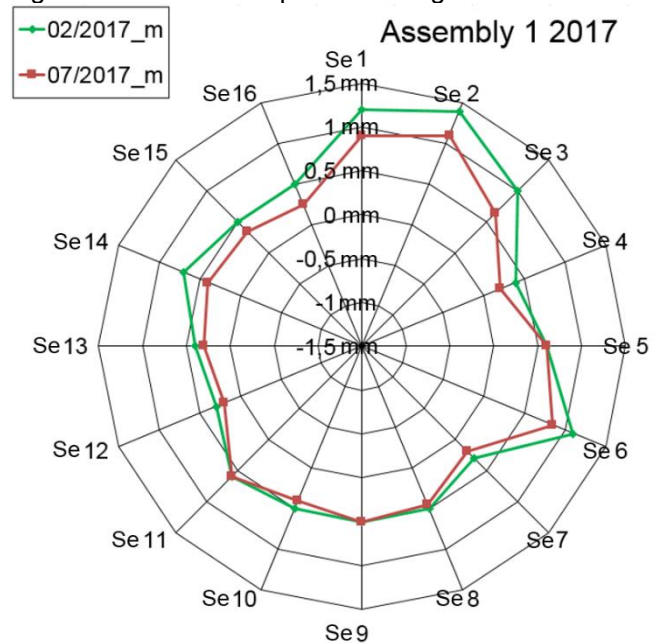

Figure 1: Radial shadowing of assemblies relative to their neighboring ones before (green) and after (red) the experimental campaign 02/2017 – 07/2017

As of 2017, the assembly 1 consists of a support structure (Fig. 2 (1)) which holds two cooling plates (2). A pipe (3) for the cooling water is attached to these cooling plates. The cooling water is fed through a flange (4a) into the pipe and exits the assembly through a second flange (4b). Both flanges are mounted to the support structure. Each assembly holds eight tungsten tiles (5), four on each cooling plate. A 2 mm sheet of Papyex (6) between the tiles and the cooling plate serves as thermal conductor. The tiles and the Papyex are firmly pulled against the cooling plates by clamps above (7a) and below (7b) the tiles. The assembly 1 is held in place by the two water flanges which are attached to an underlying frame and by two sockets (left (8b) and right (8a)) which are mounted directly to the vacuum vessel. The frame itself is also attached to the AUG vacuum vessel. Except the tiles and the Papyex,

1 all components of the assembly 1 are made from
2 stainless steel, as is the supporting frame.
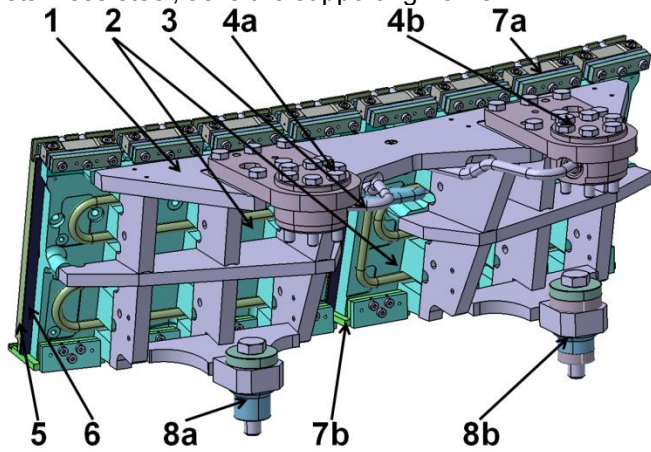
3 Figure 2: CAD model of 2017 assembly 1 with the support
4 structure (1), cooling plates (2), cooling pipe (3), water
5 flanges (4a, 4b), tungsten tiles (5), Papyex (6), clamps (7a,
6 7b) and sockets (8a, 8b)

8 The sockets of the assembly 1 have undergone a series
9 of modifications due to installation space and to prevent
10 movement. These different versions, in which no socket,
11 one socket or both sockets are electrically insulated, are
12 represented in the simulated cases.
13 The reason for this movement is suspected to be jxB
14 forces resulting from induced currents during
15 disruptions. Other reasons for the displacement like
16 thermal stress or halo currents are not investigated
17 since the temperature of the support structure is never
18 elevated significantly and halo currents create a uniform
19 force on the assembly, which would result an increased
20 shading of one neighboring assembly and a decreased
21 shading of the other one. The investigation of the eddy
22 currents and their effect on the assembly are described
23 in this paper. This includes the electromagnetic model
24 to calculate the forces and torques on the assembly 1
25 and a finite element model to simulate the displacement
26 of the assembly.

27

II. ELECTROMAGNETIC MODEL

29 This analysis was carried out in ANSYS Maxwell. A full
30 3D model of the AUG coil system was used for this
31 investigation, consisting of 16 toroidal field coils, 5
32 ohmic heating coils, 12 vertical field coils and 4 outer
33 and 2 inner control coils [6]. The space between the
34 single coils and between the coils and the divertor
35 assembly was set to be vacuum. All boundaries were
36 regarded as insulated. The material of the coils was set
37 to copper. The plasma was represented by a perfectly
38 conducting coil with one single winding. This filamentary
39 model is an approximation, since the plasma itself
40 experiences no force during the simulation. A different
41 approach [7] using CarMa0NL has shown good results.
42 Typical static values were used for the currents in the
43 coils except for the currents in the plasma $I_P(t)$ (Eq. 1)
44 and the inner control coils $I_C(t)$ (Eq. 3). The current
45 decay time constant of the plasma current τ_P (Eq. 2) was
46 set to create a certain change of the poloidal magnetic
47 field.
48 The initial plasma current $I_{P,0}$ was set to 1.6 MA and the
49 plasma dimensions a and b were set to 0.5 m and 0.8
50 m. The change rate of the poloidal magnetic field $\dot{B}_p$ was
51 set to increase from 50 T/s to 200 T/s in steps of 25 T/s.
52 The time constants were derived from the average

53 current decay times for the single B_p change rates. The
54 relation between the poloidal magnetic field and the
55 plasma current, using the mean plasma radius $\sqrt{a \cdot b}$,
56 was used to determine the current decay times. Spacial
57 variations of the plasma were neglected.
58

$$I_P(t) = I_{P,0} \cdot e^{t/\tau_P}$$	(1)
$$\tau_P = \frac{I_{P,0} \cdot \mu_0}{\ln\left(\frac{1\,A}{I_{P,0}}\right) \cdot \dot{B}_p \cdot 2\pi \cdot \sqrt{a \cdot b}}$$	(2)
$$I_C(t) = 1A \cdot e^{t/\tau_C}$$	(3)
$$\tau_C = \frac{I_{P,0} \cdot \mu_0}{\ln\left(\frac{20000\,A}{1\,A}\right) \cdot \dot{B}_p \cdot 2\pi \cdot \sqrt{a \cdot b}}$$	(4)

59

60 The currents in the inner control coils were set to rise
61 exponentially during the current quench to a value of 20
62 kA. The first 3 ms of the current quench were simulated
63 with a time step width of 0.05 ms. The mesh was
64 generated with adaptive cell length. The cells were set
65 to be tetrahedral with an angle between 50° and 60°. A
66 nonlinear residual of 0.005 was set as convergence
67 criterion for each time step.
68 A simplified model of the assembly 1 was placed into
69 the coil model together with the underlying frame and a
70 slice of the vacuum vessel. Toroidal currents were thus
71 suppressed. Measurements show a peak toroidal
72 current of 350 kA in the vessel. This creates an
73 additional magnetic field of 11 mT at the position of the
74 divertor assembly, resulting in additional forces of up to
75 700 N on the support structure and up to 500 N on the
76 tiles, depending on the case. Hence, the following
77 results underestimate the magnitude of the force due to
78 the suppressed toroidal currents. The materials of the
79 tiles and the sockets were changed according to the
80 investigated case. Seven different cases were
81 simulated:
82   1. Graphite tiles, stainless steel clamps, both
83   sockets isolated (1997-2013)
84   2. Tungsten tiles, stainless steel clamps, left
85   socket isolated (2015-2018)
86   3. Tungsten tiles, stainless steel clamps, right
87   socket isolated (2015-2018)
88   4. Tungsten tiles, stainless steel clamps, both
89   sockets conducting (2014-2015)
90   5. Tungsten tiles, titanium clamps, left socket
91   isolated
92   6. Tungsten tiles, titanium clamps, both sockets
93   isolated (new 2018)
94   7. Tungsten tiles, titanium clamps, both sockets
95   conducting
96 The first four cases represent the original version of
97 assembly 1 and the modifications to tiles and sockets.
98 Case 2, being the most recent setup, will be used as
99 reference. The last three cases were investigated as
100 options and case 6 was implemented in the 2018
101 maintenance break.
102 Fig. 3 shows the time traces of the force in x-direction
103 for each component. The traces are similar for all cases
104 and poloidal field variations. This is also true for the
105 torques. However, magnitude and direction of the forces
106 and torques change depending on the change rate of
107 the poloidal magnetic field, the material of the
108 tiles/clamps, as well as which socket is insulated. These

highest loads occurred within the first 0.5 ms of the current quench for all cases and current quench times. A 10 ms simulation revealed no further peak loads. Delayed electromagnetic transients of the structures were neglected.

Fig. 4 shows the results for the maximum total forces (a) and torques (b) on the assembly, the frame and the tiles for all cases at $\dot{B}_p$ = 200 T/s. It can be seen that case 1 has the lowest forces in all components. For the tiles, this is due to the higher electrical resistivity of graphite compared to tungsten. The forces in the assembly and the frame are low compared to case 2 because of the absence of current loops. The low torque on the assembly supports this. In case 2 the forces on the tiles which are located at the sides of the cooling plates (1, 4, 5, 8) are strongly elevated.
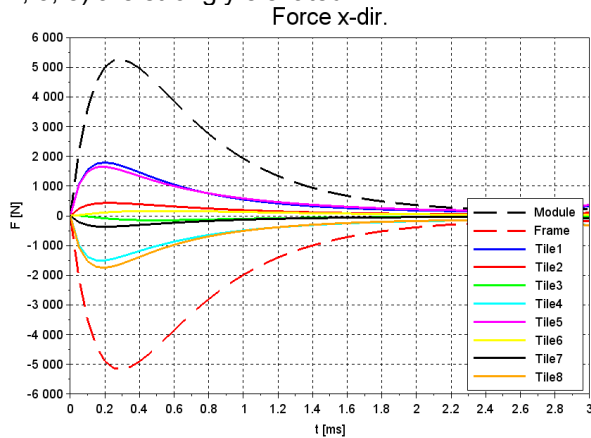

Figure 3: Time traces of the force in x-direction acting on the single components for case 5 at at $\dot{B}_p$ = 200 T/s

This is caused by two current loops, which run from the cooling plates through the outmost clamps, and tiles back into the cooling plates (Fig. 5a). This parasitic current in the outer tiles gives rise to this strong jxB force. A second current loop, running from the support structure through the right socket, the vacuum vessel and the frame back into the structure (Fig. 5b), is responsible for the strong forces on the assembly and the frame, as well as the higher torque on the assembly. A similar behavior can be seen in case 3. Forces and torques on the tiles are very similar. The forces on the frame and the assembly are lower than in case 2 because the current loop is now running through the left socket, counteracting independent eddy currents in the components. In case 4 forces and torques on the tiles are again close to the values in case 2. The forces on the assembly and the frame however are strongly reduced compared to case 2. Reason for this is that the current loop is now running through the entire length of the support structure, through both sockets and the vacuum vessel. The current is therefore highly symmetrical in the assembly and the frame which results in very low forces. However, the strongest torques occur in this case as the current loops are very large compared to all other cases. In case 5 the forces on the tiles are significantly reduced. This due to the higher electrical resistivity of the titanium clamps which reduce the parasitic current. The influence on the torques on the tiles is not as pronounced. This indicates that these torques are dominated by the eddy currents in the tiles. The forces and torques on the assembly and the frame in this case are on the same level as in case 2 as the same current loop occurs. Case 6 shows the same reduced tile forces due to the titanium clamps as

in the previous case. Forces and torques are similar the values in case 1. This is because both cases have isolated sockets and therefore no current loops. Case 7 also proves the effect of the titanium clamps on the tile forces. Concerning forces and torques on the assembly and the frame it can be seen that the same levels are reached as in case 4. This is again due to the large current loop through both sockets, the entire support structure and the vacuum vessel.
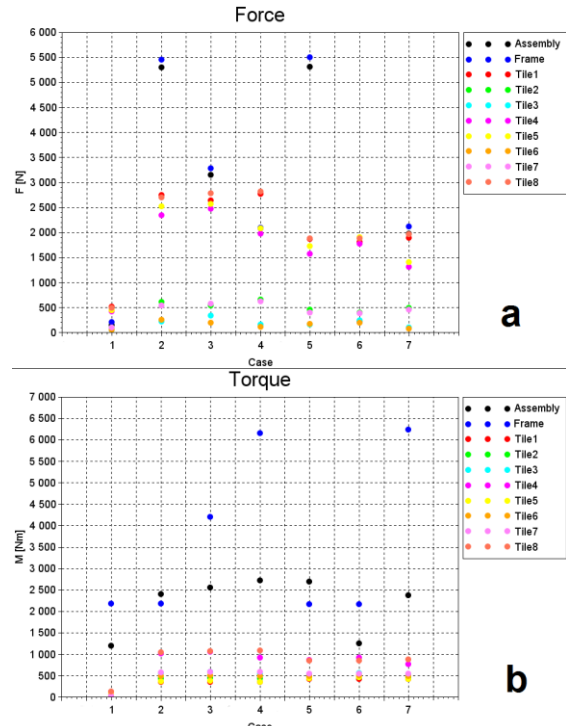

Figure 4: Maximal total forces (a) and torques (b) during current quench on assembly, frame and tiles for various cases at $\dot{B}_p$ = 200 T/s
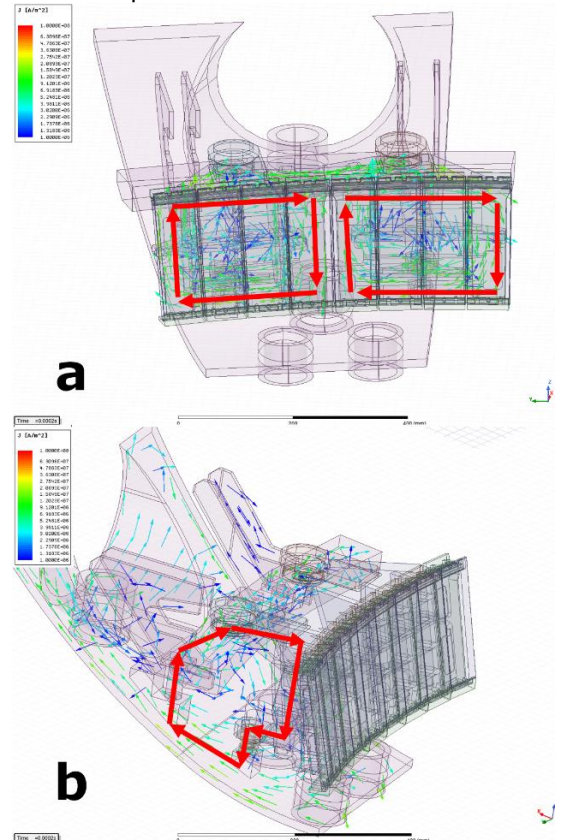
Figure 5: Current loops in the cooling plates/tiles (a) and current loops in the assembly/frame (b) for case 3 at $\dot{B}_p$ = 200 T/s

Forces (Fig. 6) and torques become stronger with increasing $\dot{B}_p$. The increase of forces and torques becomes smaller at high $\dot{B}_p$ though. This asymptotic behavior is due to the B-field, which is generated by the induced current itself. This secondary B-field is established while the poloidal field decays, compensating parts of the poloidal field change.
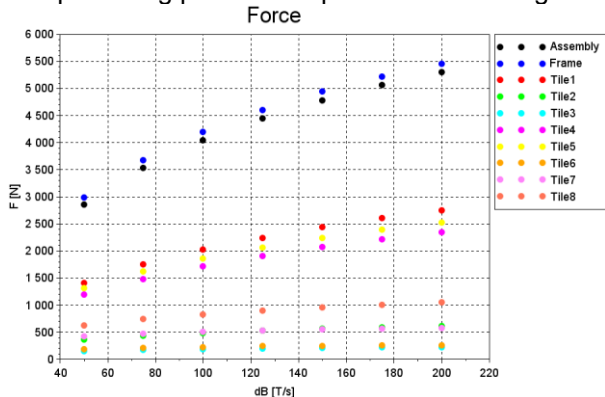
Figure 6: Maximal total forces during current quench on assembly, frame and tiles for case 2 at various $\dot{B}_p$

III. FINITE ELEMENT MODEL

This investigation was done in ANSYS transient structural environment. The simplified 3D model of the assembly 1 one was used with the materials according to the cases. The water flanges were set to be fixed while the sockets had a friction boundary condition with the friction coefficients of stainless steel (0.2) or SiN (0.12) depending on the case. The normal force on the sockets was set to 60 kN. The time traces of the forces and torques were imported from the electromagnetic results. The maximal edge length of the tetrahedral mesh was set to be 5 mm, approximating the mesh from electromagnetic analysis. The time step was set to be 0.05 ms and the total simulation was 3 ms to agree with the temporal resolution of the EM calculation. A direct solver was used and the convergence criteria were adapted by the solver during calculation.
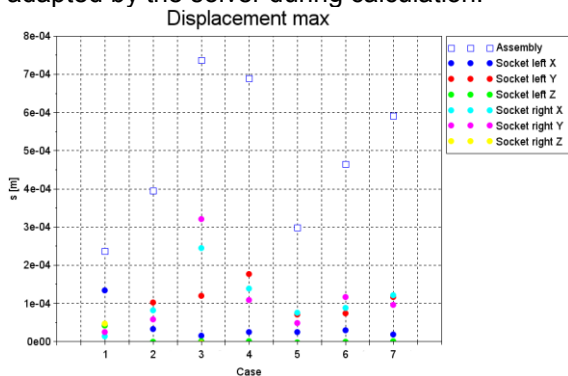
Figure 7: Maximal displacements of the assembly and the sockets for the different cases at $\dot{B}_p$ = 200 T/s

Fig. 7 shows the maximal displacements for the entire assembly and the sockets for the different cases and for different $\dot{B}_p$ in case 2. It can be seen that in all cases movement of the sockets in z-direction is widely suppressed by the normal force while displacement in radial (x) and toroidal (y) directions occur regardless of the material pairing at the sockets. This indicates that the friction force at the sockets plays a minor role compared to the forces acting on the assembly. A correlation between the displacement and the forces and torques shown in Fig. 4 cannot be seen. This is because the directions of the forces and torques

coincide in cases 3, 4, 7, leading to larger displacements, while differing in cases 2, 5.
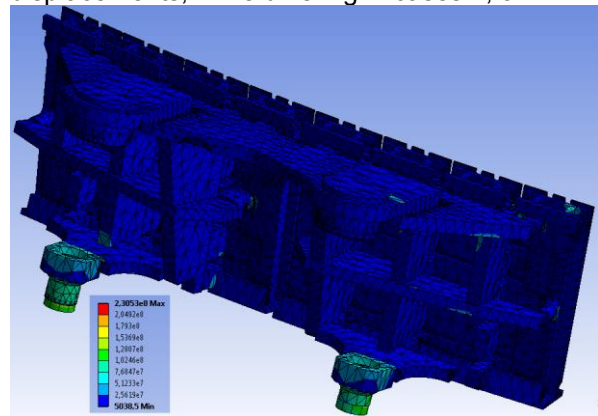
Figure 8: Peak equivalent stress in the assembly during current quench for case 5 and $\dot{B}_p$ = 200 T/s

Fig. 8 shows the peak equivalent stress on the assembly for case 2 and a poloidal magnetic field change of $\dot{B}_p$ = 200 T/s. It can be seen that the highest stress occurs in the sockets. With a peak value of 179 MPa and an average stress of 120 MPa it is well below the yield strength of 210 MPa for the material.

IV. CONCLUSION AND OUTLOOK

The movement of assembly 1 of the AUG divertor has been investigated using a 3D transient model for calculating electromagnetic forces and torques. The results pointed out current loops inside the assembly and through the surrounding structures which give rise to forces up to 5.5 kN. The friction coefficients between SiN and stainless steel were determined to be 0.18/0.16 for F_N <= 5 kN and 0.12/0.11 for F_N > 5 kN. With the forces and torques from the electromagnetic calculation and the friction coefficients, a finite element calculation was performed. The results show large displacements in cases with current loops through surrounding structures. It was decided to implement case 6 for the experimental campaign 2018 as it promises the largest reduction of forces and torques on the assembly and the frame. Both sockets of the assembly 1 are isolated from the vessel to suppress current loops. Furthermore, the stainless steel clamps are replaced with clamps made of titanium Grade5 to reduce the parasitic current through the tiles.

REFERENCES

[1] K. Krieger, H. Maier, R. Neu, Conclusions about the use of tungsten in the divertor of ASDEX Upgrade Journ. Of Nucl. Mat. Vol **266-269** (1999), p. 207-216, https://doi.org/10.1016/S0022-3115(98)00890-3

[2] M.A. Mahdavi, S.L. Allen , D.R.Baker, B. Bastasz , N.H.Brooks, Divertor heat and particle control experiments onthe DIII-D tokamak, Journ. Of Nucl. Mat. Vol **220-222** (1995), p. 13-24, https://doi.org/10.1016/0022-3115(94)00443-9

[3] R. Neu, K. Asmussen, K. Krieger, A. Thoma, H-S Bosch, The tungsten divertor experiment at ASDEX Upgrade, Plasma Phys. Contr. Fusion **38** (1996), A165-A179, https://doi.org/10.1088/0741-3335/38/12A/013

[4] R. Neu, M. Balden, V. Bobkov, R. Dux, O. Gruber, Plasma wall interaction and its implication in an all tungsten divertor tokamak, Plasma Phys. Contr. Fusion **49** (2007), B59-B70, https://doi.org/10.1088/0741-3335/49/12B/S04

[5] A. Herrmann, H. Greuner, N. Jaksic, M. Balden, A. Kallenbach, Solid tungsten Divertor-III for ASDEX Upgrade and contributions to ITER, Nucl. Fusion **55** (2015), 063015, https://doi.org/10.1088/0029-5515/55/6/063015

[6] B. Streibl, P. Lang, F. Leutner, J. Noterdaeme, A. Stäbler, Chapter 2: Machine Design, Fueling, and Heating in ASDEX Upgrade, Fus. Sc. and Tech. **44** (2003), 578-592, https://doi.org/10.13182/FST03-A400

[7] V.D. Pustitov, G. Rubinacci,, F. Villone, On the computation of the disruption forces in tokamaks, Nucl. Fusion. **57** (2017), 126038, https://doi.org/10.1088/1741-4326/aa8876